POLITECNICO DI TORINO
Repository ISTITUZIONALE

Ta/CoFeB/MgO analysis for low power nanomagnetic devices

(Article begins on next page)

16 July 2022

F. Riente, S. Mendisch, L. Gnoli, V. Ahrens, M. Ruo Roch, and M. Becherer

View Online   Export Citation   CrossMark
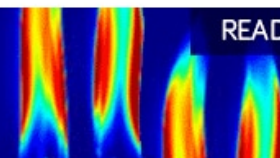
ARTICLES YOU MAY BE INTERESTED IN

Ta/CoFeB/MgO analysis for low power nanomagnetic devices

View Online   Export Citation   CrossMark

F. Riente,[1,a]   S. Mendisch,[2]   L. Gnoli,[1]   V. Ahrens,[2]   M. Ruo Roch,[1]   and M. Becherer[2]

AFFILIATIONS

[1] Department of Electronics and Telecommunications Engineering, Politecnico di Torino, 10129 Turin, Italy
[2] Department of Electrical and Computer Engineering, Technical University of Munich, Arcisstr. 21, 80333 Munich, Germany

Note: This paper was presented at the 65th Annual Conference on Magnetism and Magnetic Materials.
[a] Author to whom correspondence should be addressed: fabrizio.riente@polito.it

ABSTRACT

The requirement of high memory bandwidth for next-generation computing systems moved the attention to the development of devices that can combine storage and logic capabilities. Domain wall-based spintronic devices intrinsically combine both these requirements making them suitable both for non-volatile storage and computation. Co\Pt and Co\Ni were the technology drivers of perpendicular Nano Magnetic Logic devices (pNML), but for power constraints and depinning fields, novel CoFeB\MgO layers appear more promising. In this paper, we investigate the $Ta_2\backslash CoFeB_1\backslash MgO_2\backslash Ta_3$ stack at the simulation and experimental level, to show its potential for the next generation of magnetic logic devices. The micromagnetic simulations are used to support the experiments. We focus, first, at the experimental level measuring the switching field distribution of patterned magnetic islands, M_s via VSM and the domain wall speed on magnetic nanowires. Then, at the simulation level, we focus on the magnetostatic analysis of magnetic islands quantifying the stray field that can be achieved with different layout topologies. Our results show that the achieved coupling is strong enough to realize logic computation with magnetic islands, moving a step forward in the direction of low power perpendicularly magnetized logic devices.

I. INTRODUCTION

The increasing demand of processing power of modern computing systems moved the attention to develop solutions to mitigate the impact of the so called memory-wall.[1] In this scenario, technologies that can combine storage and logic capabilities are becoming very attracting. Perpendicular Nano Magnetic Logic (pNML) is one of the promising beyond CMOS technologies listed in the International Roadmap for Devices and Systems (IRDS 2017)[2] capable of providing both these features. pNML is a technology in which the information, encoded in non-volatile magnetic states, is elaborated and transmitted exploiting the magnetic dipole coupling between adjacent elements. The materials employed are characterized by a strong perpendicular magnetic anisotropy. Among the domain wall-based technologies, pNML is the most mature, providing a functional complete set of logic gates, memory and logic capabilities. In recent years, the correct operation of logic gates,[3] devices such as full adder,[4,5] multiplexer[6] and memory elements[7] have been

experimentally demonstrated. In addition, the fabrication process offers monolithic 3D integration.[3,8]

The propagation of information requires the superposition of the coupling field from neighboring magnets and an external out-of-plane magnetic field. These two contributions enable the magnetization reversal. The applied clocking field varies periodically in both positive and negative direction to allow both stable magnetization states to propagate. Finally, to define the propagation direction and enhance its efficiency a weak spot in the material is artificially generated. Such zone is called artificial nucleation center (ANC) and can be defined with a local Focused Ion Beam (FIB) irradiation with Ga^+ ions during the fabrication process.[9] Other mechanisms for propagation are possible involving local currents, in place of global magnetic fields for magnetization reversal.[10,11]

The first experimental realizations of pNML devices were obtained on Co\Pt multilayer films.[4,5,7,9] The film structure composed of many repetitions of Co\Pt bilayers makes it possible to reach a strong coupling between neighboring elements. In addition,

the stack characteristics can be locally tuned by means of ion irradiation techniques to generate ANCs for controlled domain wall (DW) nucleation.[9] The main limitation of this configuration is the required clocking field to obtain a correct propagation of information that showed values above 50 mT with quasi-static fields.[4] The intensity of the external magnetic field impacts heavily on the energy budget of the circuit. The overall power consumption depends almost exclusively on the required clocking field and on the efficiency of the generation circuit. A forecast on the power dissipation of an on-chip clocking scheme sandwiched in a soft-magnetic cladding showed that the maximum required amplitude should fall below 20 mT.[12,13] In the literature, other thin film configurations with strong perpendicular anisotropy have been presented and studied for spintronic devices. Co\Ni thin films showed to be promising due to the perpendicular anisotropy and the possibility to locally tailor their characteristics via ion beam irradiation.[13,14] Another promising solution is represented by the CoFeB\MgO stacks. They show a strong magnetic anisotropy and fast magnetic dynamics. Moreover, the perpendicular anisotropy, arising at the ferromagnet-oxide interface, can be finely tuned during the fabrication and modulated with electric fields.[15,16] They received great attention for the excellent compatibility with magnetic tunnel junction in which they are used both as free and reference layer.[17–19] These stacks have also been integrated with CMOS technology to realize high speed magnetic memories.[20–22] CoFeB\MgO stacks have the potential to be also a good candidate for the development of low power nanomagnetic logic devices. In this paper, a $Ta_2\backslash CoFeB_1\backslash MgO_2\backslash Ta_3$ stack, with alloy composition $Co_{20}Fe_{60}B_{20}$, is investigated. The presented study examines in depth its applicability for nanomagnetic logic both at the experimental and simulation level. In section II, the experimental setup and experimental measurements are presented. In section III, the micromagnetic simulation are described and the main outcomes are presented, with particular attention to the layout topology of the logic gates. Finally, section IV concludes the paper summarizing the results and presenting future perspectives for the presented structures.

II. EXPERIMENTS

Nanomagnetic structures made from Ta\CoFeB\MgO thin films with perpendicular magnetic anisotropy are fabricated and subsequently characterized, assessing their eligibility for advanced pNML concepts. The individual layers (thicknesses given in nanometer) are deposited onto silicon (100) substrates, featuring an oxide layer of $\approx$ 50 nm thickness, via confocal rf-magnetron sputtering (base pressure $< 2\times10^{-7}$ mbar). The power density applied to the 2-inch targets is constant for all materials (0.5 W cm^{-2}). The same holds for the working pressure (4 μbar $\approx$ 3 mTorr), except for the MgO, which is sputtered from a compound target at 2 μbar ($\approx$ 1.5 mTorr). After the deposition, the samples are annealed for 10 min at 550 K in a nitrogen atmosphere to set the PMA to the desired $\approx 5\times10^5$ J m^{-3}. The magnetic properties (also the simulation parameter) of the used $Ta_2\backslash CoFeB_1\backslash MgO_2\backslash Ta_3$ stack are derived from vibrating sample magnetometer measurements (K_u is calculated via the area method) and cross-checked via broadband ferromagnetic resonance spectroscopy.

To realize the desired test structures, a sample with the same stack configuration is further processed. First, focused ion beam (FIB) lithography (using PMMA as a positive E-beam resist) is used to define the structure layouts. The deposition of a 5 nm thick Ti layer is then combined with a lift-off process to create the necessary hard mask for the subsequent Ar^+ ion-beam milling step, which removes all material but the earlier defined layouts. The on-chip field coils are realized in the last step via conventional optical contact lithography together with the deposition of a Cu metal layer ($\approx$ 750 nm) and a second lift-off process. An overview of the final design is depicted in figure 1. The test-structures (400 nm wide wires for DW-velocity, and 1 μm wide disks for coercivity measurements) are analyzed statically as well as in the time domain via stroboscopic Wide-field Kerr-microscopy (WMOKE), synchronizing magnetic field pulses in the ns-range with the image acquisition of a high dynamic range sCMOS camera. Ultra short magnetic field pulses are generated via on-chip coils with a single winding, as illustrated in figure 1. To reach pulse widths down to the single digit ns-range, a low-side switch in combination with a fast gate diver is used to discharge a capacitance through the on-chip coils. The gate driver is thereby addressed by an Agilent 81112A Pulse Generator.

A. Coercivities

The coercivity of single domain magnets is in contrast to films domianted by the nucleation field, $H_c \approx H_{nuc}$ presuming that the domain wall (DW) depinning fields are much lower ($H_{depin} \ll H_{nuc}$). It is furthermore important to differentiate between coercivities measured at quasi-static fields from those measured at short time scales of microseconds and below. The magnetization reversal process of single-domain magnets is comprised of two phases. Following the initial DW nucleation, at a point of lowered anisotropy, the DW must propagate through the entire structure to complete the reversal. For this propagation to happen, the DW, however, must first overcome the anisotropy gradient at the nucleation site
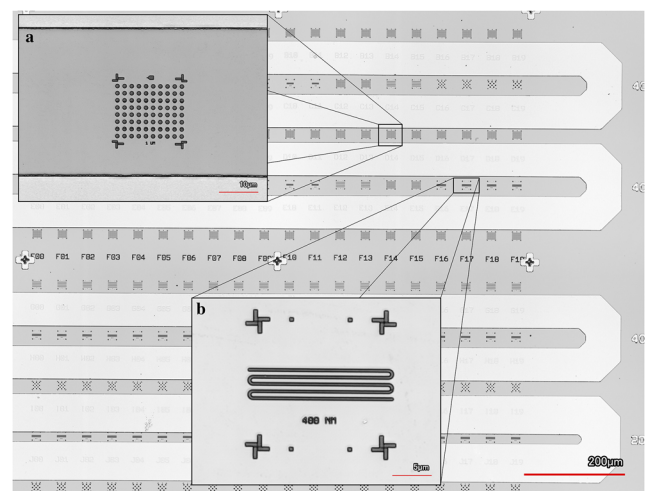
FIG. 1. Optical micrograph of the $Ta_2\backslash CoFeB_1\backslash MgO_2\backslash Ta_3$ sample. The on-chip coil has been fabricated on top of structured magnets to measure both the domain wall speed and the switching field distribution. **a**, Zoom of the patterned nano-disks. **b**, Zoom of the patterned snakes for the domain wall velocity measurements.
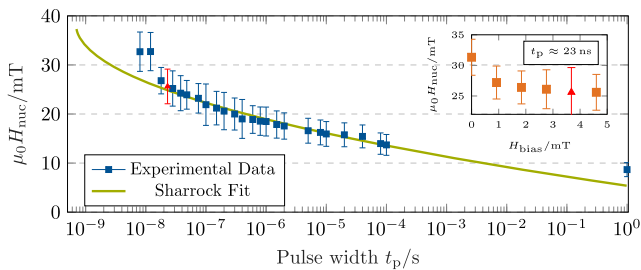
and depin. It is therefore, important to differentiate and consider both the nucleation as well as the propagation time separately ($t_{switch} \approx t_{nuc} + t_{prop}$). The timescales for the nucleation process are governed by the Arrhenius-Néel law, from which the so-called Sharrock formalism can be derived. It describes the external field necessary to switch a single domain magnet with at least 50 % probability within a certain time. This threshold mark is defined as

$$H_{sw} = H_{s0}\left[1 - \left(\frac{k_B T}{E_0}ln\left(\frac{f_0 t_p}{ln(2)}\right)\right)^{(1/2)}\right], \qquad (1)$$

with H_{s0} as the switching field at 0 K, f_0 as the attempt frequency ($\approx 1\times10^9$ Hz) and $E_0 = K_u V$ as the energy barrier without field equal to the product of anisotropy and volume.[23]

For the quasi-static case, the switching field distribution (SFD) is calculated from a data-set of 1600 nano-disks resulting in a mean coercivity of $H_{c,mean} = (8.67\pm0.06)$ mT, and a narrow FWHM SFD of only $\sigma_{FWHM} = (2.87\pm0.10)$ mT. This is a significant reduction in the absolute as well as relative SFD even compared to the recently evaluated low anisotropy Co\Ni multilayers.[13] The most plausible explanation for this is the amorphous structure of CoFeB layers annealed at low temperatures.

Figure 2 displays the time evolution of H_{sw} for timescales ranging from the quasi-static case down to the single-digit ns-range according to the guidelines in Ref. 12. H_{sw} is determined for 80 nano-disks with the FWHM of the SFDs displayed as error bars. The obligatory fit, according to the Sharrock formula, shows good agreement with the collected data down to timescales below 100 ns. Here, several effects start to affect the measurements. For very short pulses, the time is not sufficient to propagate the DW through the entire magnet, leading to detection errors within the optical readout system. This, however, can be resolved by applying a ms-range field pulse with a low amplitude (≈ 3 mT) after every nucleation pulse. However, below 50 ns, we propose another mechanism leading to a measured deviation from the Arrhenius behavior. Depending on the properties of the nucleation site, the timescales might be too short for the domains to stabilize, resulting in a back-flip of the magnetization. This behavior, however, should be very sensitive to constructive bias fields, as the additional energy helps to stabilize the nucleated domains. The inlet of figure 2 displays the measured coercivities

depending on the applied bias field. H_{sw} is thereby corrected by the amplitudes of the bias field. As proposed, the measured coercivities are reduced significantly even for small bias fields, after which a plateau is formed, indicating the inhibition of possible back-flipping events.

The time-dependent nucleation probability follows an Arrhenius model at least down to pulse widths of ≈ 20 ns. A fit, according to the Sharrock formalism shows good agreement, with the fitting parameters converging to $H_{s0} = (38.23\pm1.50)$ mT and $E_0 = \frac{k_B T}{28.57} \pm \frac{k_B T}{2.2}$. Considering the relatively high anisotropy of the film ($K_{eff} \approx 1.3\times10^5$ J m^{-3}), these are very encouraging results, rivaling those of heavily optimized Co\Ni multilayers.[13]
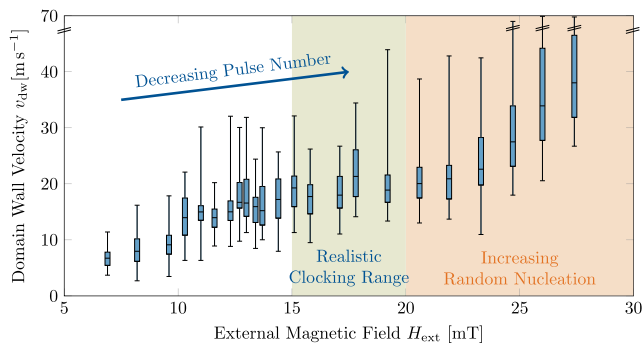
B. DW-velocities

Nucleation is only one part of the reversal process. Equally relevant is the rapid expansion and propagation of the DW through the magnet. Similar to electronic circuits, the slowest path determines the maximum operating frequency. Hence it is possible to estimate upper limits for the clocking frequencies f_{clk} for the used feature size, given the design and DW velocity v_{DW}. DW motion can, roughly speaking, be separated into two distinct domains. At low fields, DW depinning heavily depends on thermal activations, thus resulting in a slow probabilistic creep motion. However, this motion is no longer affected by pining and depinning events at high fields, leading to flow like motion, with v_{DW} linearly depending on H. For applications, the creep regime is generally considered irrelevant, due to the low velocities $\ll 1$ m s^{-1}.

In order to assess the DW velocities of the Ta\CoFeB\MgO thin film, DWs were propagated through 400 nm wide nano-wires (example depicted in figure 1) by bursts of 25 ns long field pulses with varying amplitudes. First of all, very short pulse widths were chosen to limit random nucleation events inside the nanowires and second, to mimic typical clock-cycle lengths. The number of bursts was adjusted between 1 and 10 to keep the mean DW-displacement above ≈ 1 µm to reliably identify the displacements. The actual velocities can then be calculated from the pulse-width dependent DW displacements.

Figure 3 depicts the measured DW-velocity distributions for fields up to 28 mT as box plots. The depinning field in these nanowires at quasi-static fields is in the range of 0.3 mT. However, reliable measurements in the creep regime are extremely difficult considering pulse widths below 1 µs. Data can be gathered starting at ≈ 7 mT. The measurements show a clear initial increase in DW-velocity, plateauing between 13 mT and 22 mT, before increasing again from 22 mT on-wards. The observed plateau may result from the decreasing velocities above the Walker-breakdown.[24] The Walker-breakdown, calculated to occur below 1 mT for this material system, is masked by the creep motion. The second velocity increase above 22 mT, could mark the onset of flow motion. However, the wide distribution of the collected data suggests some form of intermediate flow in which large pinning sites still dominate. Reliable data for higher fields could not be collected due to the increasing amount of random nucleation events. For possible applications, the relevance of very high fields is, of course, also limited. Considering clock fields around 20 mT and a feature size of $l_{max} = 400$ nm as simulated below, it is possible to estimate clock frequencies around 20 MHz. For a scaled architecture (feature sizes < 100 nm)

FIG. 2. Calculated nucleation fields (H_{nuc}) as a function of the applied pulse width. The data is completed by a fit according to the Sharrock formalism (equation 1) with an attempt frequency of 1 GHz, $E_0 = \frac{k_B T}{28.5}$ and $H_{s0} = 38.2$ mT. The error bars indicate the FWHM of the SFD for the 80 measured nano-disks. For the quasi-static case, the approximation $H_{nuc} \approx H_c$ is used.

FIG. 3. Box plot of the field dependent median DW velocities (v_{DW}), each extracted from more than 30 measurements. Measured by propagation of a DW through a 400 nm wide nanowire by external, 25 ns long field pulses of varying field strength H_{ext}. Field regimes proposed for on-chip clocking (green) and where random nucleation occurs (orange) are marked in the plot. Note the y-axis discontinuity for the high whiskers.

frequencies in range of a few hundred MHz seem feasible, even considering to further optimization regarding DW mobility.

III. SIMULATIONS

The data from the experiments showed low coercivity and high perpendicular magnetic magnetic anisotropy, comparable with the one obtained with Co\Ni multilayer stacks. This makes Ta\CoFeB\MgO films very appealing for logic applications. We investigate two layout topologies through micromagnetic simulations, which are performed with the GPU accelerated software package mumax3.[25] The aim is to identify what layout configuration fits the needs for the development of a new family of logic gates based on Ta\CoFeB\MgO nanomagnets. The idea is to develop a robust and regular structure that can implement NAND/NOR functions according to a global or a local bias field.

The first topology consider co-planar inputs and output, whereas in the second structure the inputs are moved to another physical layer (figure 4f). Figure 4a illustrates schematically the 3D-stacked layout, with all the dimensions involved. These dimensions are valid also for the co-planar layout with the difference that the inputs are on the side of the output (wide as the gap size), separated by the inter-magnet space *y-space*. The magnetic properties of the stack are taken from the measured samples. The saturation magnetization is $M_s = 8.3 \times 10^5$ A m^{-1} and the uniaxial anisotropy constant $K_u = 5.6 \times 10^5$ J m^{-3}. The exchange constant $A = 20 \times 10^{-12}$ J m^{-1} is taken from the literature.[26] The discretization of the sample is 2.5 nm×2.5 nm×0.5 nm. A variation of 5% of the anisotropy constant was applied over the whole film. The damping constant of the CoFeB\MgO film was taken from the literature[26] and it is equal to $\alpha = 0.015$.

In the 3D layout, the two inputs are co-planar and parallel on layer 2 (L2), separated by a small gap. They partially overlap the
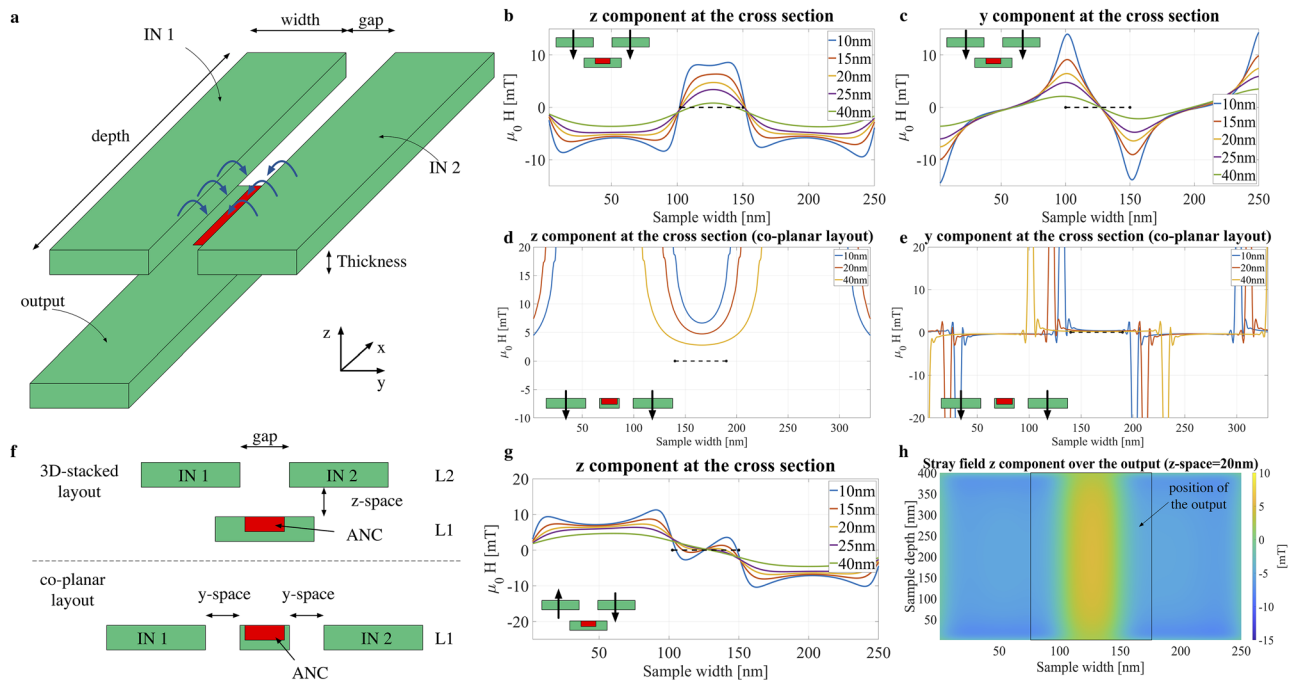
FIG. 4. a, Topology of the structure simulated to quantify the stray fields over the output magnet. **b**, Stray field (z-component) at the cross section of the output magnet at different vertical distances when both inputs are pointing downwards. **c**, Stray field (y-component) at the cross section of the output magnet at different vertical distances. **d**, Stray field (z-component) over the output magnet when the horizontal distance is varied from 10 nm to 30 nm. **e**, Stray field (y-component) at the cross section of the output magnet at different horizontal distances. **f**, Cross section of the 3D stacked (up) and the co-planar layout (down) configurations. **g**, Stray field (z-component) at the cross section of the output magnet at different vertical distances when the two inputs are anti-parallel. **h**, Stray field distribution (z-component) over the output magnet when the vertical distance is 20 nm.

output magnet lying on layer 1 (L1). In this study, the gap size is 50 nm. The output magnet is located on the first layer (L1), centered on the gap. Every input magnet has the following dimensions: width = 100 nm, depth = 400 nm and thickness = 1 nm. The stray field reaching the output magnet has been analyzed for different vertical distances (10 nm, 15 nm, 20 nm, 25 nm, 40 nm). Figure 4b shows the z-component varying the vertical space among the layers (L1 and L2) when both inputs are magnetized to the logic 0. In this configuration, the inputs are anti-ferromagnetically coupled to the output. The dashed line shows the position of the 50 nm gap, where the soft PMA spot should be defined. It is possible to observe that a vertical separation of 15 nm and 20 nm provide the best trade-off in term of coupling strength and field homogeneity at the center, in correspondence of the gap. Indeed, the coupling reaches 6.4 mT with 15 nm separation and 4.8 mT with 20 nm distance. For the 20 nm vertical distances, the out-of-plane component of the stray field over the output magnet is displayed in figure 4h. For the sake of clarity the position of the output is indicated by a black box. The yellow area identifies the region with a stronger out-of-plane field. Figure 4g illustrates the z-component when the inputs are anti-parallel. For the 20 nm distance the out-of-plane field reaching the gap is almost canceled out. Therefore, the final magnetization of the output is determined only by the bias field and the sign of the global field.

Similarly, we investigated the topology with co-planar inputs and output with horizontal spaces: 10 nm, 20 nm, 40 nm. The out-of-plane components, reported in figure 4d, shows that the coupling reaches a maximum value of 6.6 mT and 4.8 mT for 10 nm and 20 nm respectively. However, even if the coupling appears strong enough also for these configurations, the planar layout cannot be successfully adopted for performing logic operations. The z-component is stronger on the edges weaker at the center, where the nucleation center is supposed to be located. This can favor the domain wall nucleation from edges instead of starting from the center of the output magnet. The in-plane component for the three distances is reported in figure 4e. It is possible to identify the position of the two inputs, starting in correspondence of the peaks. When the horizontal distance is below 10 nm (figure 4e) the in-plane component of the inputs combined with the strong z-component on the edges may initiate the magnetization reversal. The dashed line in figure 4.d-e show the size and position of the 50 nm gap.

Therefore, the 3D-stacked layout appears more promising in term of field distribution and feasibility of the fabrication process. In the pNML technology, the logic computation is achieved by the superposition of the dipole coupling of adjacent nanomagnets and the global out-of-plane field. Here, in addition to that a bias field is introduced. The bias field can be locally generated by a third input magnet located under the output or globally generated by adding a bias to the clocking field. The bias field defines the logic function implemented by each gate, whereas the global clocking field starts the computing phase. The bias field acts as a third input and can program all the gates (global bias) at once, or every gate independently (local bias) in the logic architecture to operate as NAND/NOR gate. The global bias field can be seen as a virtual input, since it will not be physically present in the design, but it defines the logic function of every gate. Table I summarizes the truth table of the logic gate. It is possible to observe that it virtually operates as a majority with only

TABLE I. Truth table of the proposed two inputs logic gates. It can operate as NAND/NOR according to the sign of the bias field.

Bias	IN1	IN2	OUT	Function
0	0	0	1	
0	0	1	0	
0	1	0	0	NOR
0	1	1	0	
1	0	0	1	
1	0	1	1	
1	1	0	1	NAND
1	1	1	0	

two physical inputs. The sign of the bias field determines the logic function implemented.

IV. CONCLUSIONS

In this paper, we have investigated the $Ta_2\backslash CoFeB_1\backslash MgO_2\backslash Ta_3$ stack from the perspective of developing a new family of perpendicular magnetic logic devices. The low coercivity, below 10 mT and high perpendicular magnetic anisotropy make the material very appealing for memory and logic applications with low energy computing capabilities. The measurements exhibit faster domain wall motion and narrower FWHM SDF if compared to Co\Pt and Co\Ni films. Our simulation results show that a vertical separation ranging between 15 and 20 nm provides enough coupling for implementing two inputs NAND/NOR gates. Moreover, we demonstrated that the 3D-stacked layout is preferable in order to reach the maximum coupling strength at the center of the output magnet. The proposed solution makes it possible to design NAND/NOR gate with only two physical inputs (global bias) or to individually control the logic function of each gate by a third additional input.

DATA AVAILABILITY

The data that support the findings of this study are available from the corresponding author upon reasonable request.

REFERENCES

[1] Y. Kwon and M. Rhu, "Beyond the memory wall: A case for memory-centric HPC system for deep learning," in *2018 51st Annual IEEE/ACM International Symposium on Microarchitecture (MICRO)* (IEEE, 2018), pp. 148–161.

[2] International Roadmap for Devices and Systems: BEYOND CMOS Chapter, 2017.

[3] I. Eichwald, S. Breitkreutz, G. Ziemys, G. Csaba, W. Porod, and M. Becherer, "Majority logic gate for 3D magnetic computing," Nanotechnology **25**, 335202 (2014).

[4] S. Breitkreutz, I. Eichwald, J. Kiermaier, A. Papp, G. Csaba, M. Niemier, W. Porod, D. Schmitt-Landsiedel, and M. Becherer, "1-bit full adder in perpendicular nanomagnetic logic using a novel 5-input majority gate," EPJ Web of Conferences **75**, 05001 (2014).

[5] S. Breitkreutz, J. Kiermaier, I. Eichwald, C. Hildbrand, G. Csaba, D. Schmitt-Landsiedel, and M. Becherer, "Experimental demonstration of a 1-bit full adder in perpendicular nanomagnetic logic," IEEE Transactions on Magnetics **49**, 4464–4467 (2013).

[6] G. Turvani, F. Riente, E. Plozner, M. Vacca, M. Graziano, and S. B. Gamm, "A pNML compact model enabling the exploration of three-dimensional architectures," IEEE Transactions on Nanotechnology **16**, 431–438 (2017).

[7] F. Riente, G. Ziemys, C. Mattersdorfer, S. Boche, G. Turvani, W. Raberg, S. Luber, and S. B. Gamm, "Controlled data storage for non-volatile memory cells embedded in nano magnetic logic," AIP Advances **7**, 055910 (2017).

[8] I. Eichwald, J. Kiermaier, S. Breitkreutz, J. Wu, G. Csaba, D. Schmitt-Landsiedel, and M. Becherer, "Towards a signal crossing in double-layer nanomagnetic logic," IEEE Transactions on Magnetics **49**, 4468–4471 (2013).

[9] S. Breitkreutz, J. Kiermaier, S. Vijay Karthik, G. Csaba, D. Schmitt-Landsiedel, and M. Becherer, "Controlled reversal of Co/Pt Dots for nanomagnetic logic applications," Journal of Applied Physics **111**, 07A715 (2012).

[10] D. Bhowmik, L. You, and S. Salahuddin, "Spin Hall effect clocking of nanomagnetic logic without a magnetic field," Nature nanotechnology **9**, 59–63 (2014).

[11] M. Niemier, "Clocking with no field," Nature nanotechnology **9**, 14–15 (2014).

[12] M. Becherer, J. Kiermaier, S. Breitkreutz, I. Eichwald, G. Žiemys, G. Csaba, and D. Schmitt-Landsiedel, "Towards on-chip clocking of perpendicular nanomagnetic logic," Solid-State Electronics **102**, 46–51 (2014), selected papers from ESSDERC 2013.

[13] S. Mendsich, V. Ahrens, M. Kiechle, A. Papp, and M. Becherer, "Perpendicular nanomagnetic logic based on low anisotropy Co/Ni multilayer," Journal of Magnetism and Magnetic Materials **510**, 166626 (2020).

[14] L. You, R. C. Sousa, S. Bandiera, B. Rodmacq, and B. Dieny, "Co/Ni multilayers with perpendicular anisotropy for spintronic device applications," Applied Physics Letters **100**, 172411 (2012).

[15] J. G. Alzate, P. Khalili Amiri, G. Yu, P. Upadhyaya, J. A. Katine, J. Langer, B. Ocker, I. N. Krivorotov, and K. L. Wang, "Temperature dependence of the voltage-controlled perpendicular anisotropy in nanoscale MgO| CoFeB| Ta magnetic tunnel junctions," Applied physics letters **104**, 112410 (2014).

[16] K. Miura, S. Yabuuchi, M. Yamada, M. Ichimura, B. Rana, S. Ogawa, H. Takahashi, Y. Fukuma, and Y. Otani, "Voltage-induced magnetization dynamics in CoFeB/MgO/CoFeB magnetic tunnel junctions," Scientific reports **7**, 42511 (2017).

[17] S. Ikeda, K. Miura, H. Yamamoto, K. Mizunuma, H. Gan, M. Endo, S. Kanai, J. Hayakawa, F. Matsukura, and H. Ohno, "A perpendicular-anisotropy CoFeB–MgO magnetic tunnel junction," Nature materials **9**, 721–724 (2010).

[18] B. Jinnai, K. Watanabe, S. Fukami, and H. Ohno, "Scaling magnetic tunnel junction down to single-digit nanometers—challenges and prospects," Applied Physics Letters **116**, 160501 (2020).

[19] K. Garello, F. Yasin, S. Couet, L. Souriau, J. Swerts, S. Rao, S. Van Beek, W. Kim, E. Liu, S. Kundu, D. Tsvetanova, K. Croes, N. Jossart, E. Grimaldi, M. Baumgartner, D. Crotti, A. Fumémont, P. Gambardella, and G. S. Kar, "SOT-MRAM 300MM integration for low power and ultrafast embedded memories," in *2018 IEEE Symposium on VLSI Circuits* (IEEE, 2018), pp. 81–82.

[20] K. Lee, J. H. Bak, Y. J. Kim, C. K. Kim, A. Antonyan, D. H. Chang, S. H. Hwang, G. W. Lee, N. Y. Ji, W. J. Kim, J. H. Lee, B. J. Bae, J. H. Park, I. H. Kim, B. Y. Seo, S. H. Han, Y. Ji, H. T. Jung, S. O. Park, O. I. Kwon, J. W. Kye, Y. D. Kim, S. W. Pae, Y. J. Song, G. T. Jeong, K. H. Hwang, G. H. Koh, H. K. Kang, and E. S. Jung, "1Gbit high density embedded STT-MRAM in 28nm FDSOI technology," in *2019 IEEE International Electron Devices Meeting (IEDM)* (IEEE, 2019), pp. 2.2.1–2.2.4.

[21] V. B. Naik, K. Lee, K. Yamane, R. Chao, J. Kwon, N. Thiyagarajah, N. L. Chung, S. H. Jang, B. Behin-Aein, J. H. Lim, T. Y. Lee, W. P. Neo, H. Dixit, S. K., L. C. Goh, T. Ling, J. Hwang, D. Zeng, J. W. Ting, E. H. Toh, L. Zhang, R. Low, N. Balasankaran, L. Y. Zhang, K. W. Gan, L. Y. Hau, J. Mueller, B. Pfefferling, O. Kallensee, S. L. Tan, C. S. Seet, Y. S. You, S. T. Woo, E. Quek, S. Y. Siah, and J. Pellerin, "Manufacturable 22nm FD-SOI embedded MRAM technology for industrial-grade MCU and IOT applications," in *2019 IEEE International Electron Devices Meeting (IEDM)* (IEEE, 2019), pp. 2.3.1–2.3.4.

[22] S. Aggarwal, H. Almasi, M. DeHerrera, B. Hughes, S. Ikegawa, J. Janesky, H. K. Lee, H. Lu, F. B. Mancoff, K. Nagel, G. Shimon, J. J. Sun, T. Andre, and S. M. Alam, "Demonstration of a reliable 1 Gb standalone spin-transfer torque MRAM For industrial applications," in *2019 IEEE International Electron Devices Meeting (IEDM)* (IEEE, 2019), pp. 2.1.1–2.1.4.

[23] M. P. Sharrock, "Time dependence of switching fields in magnetic recording media," Journal of Applied Physics **76**, 6413–6418 (1994).

[24] C. Burrowes, N. Vernier, J.-P. Adam, L. Herrera Diez, K. Garcia, I. Barisic, G. Agnus, S. Eimer, J.-V. Kim, T. Devolder, A. Lamperti, R. Mantovan, B. Ockert, E. E. Fullerton, and D. Ravelosona, "Low depinning fields in Ta-CoFeB-MgO ultrathin films with perpendicular magnetic anisotropy," Applied Physics Letters **103**, 182401 (2013).

[25] A. Vansteenkiste, J. Leliaert, M. Dvornik, M. Helsen, F. Garcia-Sanchez, and B. Van Waeyenberge, "The design and verification of MuMax3," AIP Advances **4**, 107133 (2014).

[26] R. Tomasello, E. Martinez, R. Zivieri, L. Torres, M. Carpentieri, and G. Finocchio, "A strategy for the design of skyrmion racetrack memories," Scientific Reports **4**, 6784 (2014).